What causes creep bursts in the Åknes landslide, Norway?

Andreas Aspaas[1,4], Pascal Lacroix[2], Clara Sena[3], Lene Kristensen[4], Nadège Langet[5], and François Renard[1,2]

[1]The Njord Centre, Departments of Geosciences and Physics, University of Oslo, Oslo, Norway

[2]ISTerre, Univ. Grenoble Alpes, Grenoble INP, Univ. Savoie Mont Blanc, CNRS, IRD, Univ. Gustave Eiffel, 38000 Grenoble, France

[3]Department of Geosciences, University of Oslo, Oslo, Norway

[4]Section for Landslides and Avalanches, Norwegian Resources and Energy Directorate, Trondheim, Norway

[5]Department of Applied Seismology, NORSAR, Lillestrøm, Norway

Corresponding author: Andreas Aspaas (a.g.aspaas@geo.uio.no)

Key Points

- We detected creep bursts on the shear zone of the Åknes landslide that accommodates 11% of the total displacement.
- Most creep bursts are caused by both the progressive wear of rock bridges and enhanced stress corrosion
- The largest creep bursts are preceded by increased water pressure and microseismicity on the shear zone.

Abstract

Slow-creeping landslides may fail catastrophically, posing significant threats to infrastructure and lives. Landslides weaken over time through rock mass damage processes that may occur by slow steady-state creep or transient accelerations of slip, called creep bursts. Creep bursts may control landslide stability by inducing short-term damage and strain localization. This study focuses on the Åknes landslide in Norway, which moves up to 6 centimetres per year and could potentially trigger a large tsunami in the fjord lying below. Here, an eleven-year dataset is compiled and analyzed, including kinematic, seismic, and hydrogeological data acquired at the landslide surface and in a series of boreholes. Creep bursts with millimetre amplitude are detected in the landslide's shear zone. An annual average of two creep burst events have been recorded within the shear zone in each borehole, accounting for approximately 11% of the total displacement. Creep bursts phased over multiple boreholes are preceded by increased seismic activity and water pressure increase. However, most creep bursts are observed in only one or a few boreholes. Creep bursts often occur during the seasonal high and low levels of groundwater, correlating with local peaks in water pressure, but no such correlation is observed during summer. We propose that on one side, the progressive wear of asperities leads to creep bursts being uncorrelated to water pressure changes. Conversely, enhanced stress corrosion causes creep bursts to correlate to water level fluctuations. Our findings offer unique insights into landslide mechanics, correlating shear zone dynamics with surface displacement and environmental parameters.

Plain Language Summary

Slow-moving landslides, advancing from millimetres to meters per year, can have strong destruction potential if they fail catastrophically. A landslide sliding plane weakens over time by rock crushing and fracturing. One of these processes is short-lived movement accelerations that we call creep bursts. Creep bursts may control landslide stability by inducing short-term damage and the development of a plane that allows the landslide to slide and collapse. This study focuses on the Åknes landslide in Norway, which moves at 6 centimetres per year and could potentially trigger a great tsunami in the fjord below. Creep bursts with millimetre movements are detected at the landslide’s sliding plane. The largest bursts are correlated with the groundwater level in the landslide, which varies with seasons. However, many small creep bursts do not show any correlation with groundwater level. Creep bursts associated with groundwater changes may be related to increased corrosion by water flow. At the same time, the gradual crushing of rock mass may cause creep bursts unrelated to water level changes. Our dataset provides quantitative insights on transient slip accelerations and these accelerations may be crucial in driving a large-scale failure of the Åknes landslide.

1 Introduction

Landslides may creep for thousands of years. They can move steadily or accelerate seasonally and/or transiently and potentially fail catastrophically (e.g., Lacroix et al., 2020). The mechanisms of landslide deformation include weathering by microcracking and subcritical crack growth (e.g., Atkinson, 1984; Dille et al., 2019), bulk damage in the rock volume (e.g., Brideau et al., 2009), and sliding along a shear plane separating the landslide from the bedrock (e.g., Agliardi et al., 2020). Sliding can be influenced by external stress variations, the geometry and distribution of displacement, and the resistance to slip, as proposed by Wesson (1988). Several mechanisms have been suggested to explain landslide failure, including strain localization within a shear zone with rate-strengthening or rate-weakening properties (Kilburn & Petley, 2003; Viesca & Rice, 2012), porosity modulations causing dilation and contraction of the shear zone (Agliardi et al., 2020; Iverson, 2005), and viscosity bifurcation or changes in shear modulus of clay layers (Mainsant et al., 2012). Sliding occurs through either stick-slip processes, aseismic deformation at a constant rate, or transient aseismic events, also called creep bursts that last from minutes to days with slips in the mm range (Finnegan et al., 2022). Several studies on various landslides have evidenced these different sliding mechanisms (Finnegan et al., 2022; Lacroix et al., 2022; Poli, 2017; Yamada et al., 2016). For instance, Finnegan et al. (2022), based on data acquired on two extensometers installed 100 m apart, showed that the Oak Ridge landslide displacement occurs by short stick-slip events of mm-scale slip over asperities less than 100 m in size. On other landslides, seismic repeaters were interpreted by the existence of stick-slip events on larger patches (Lacroix et al., 2022; Poli, 2017; Yamada et al., 2016). On subduction zones, where these two mechanisms were also detected, the fault surface is modelled by seismogenic patches surrounded by creeping segments with a strong interplay between the two (e.g., Lay and Nishenko, 2022; Jolivet et al., 2023). This model is widely used despite the direct access to active shear zones in strike-slip faults (Templeton et al., 2008) and volcanoes (Gudmundsson, 2016), typically deeper than 1 km, is challenging. However, landslides often reveal shear zones in the upper 100 meters of the Earth's crust, making them ideal natural objects to study friction and slip processes.

It has been shown that landslide motion is mostly aseismic on landslides where both local seismic arrays and displacement measurements exist simultaneously (Gomberg et al., 2011; Lacroix & Helmstetter, 2011). For instance, on the Séchilienne landslide, almost 99.9% of the slip is released aseismically (Lacroix & Helmstetter, 2011). Therefore, there is a discrepancy between the displacement data and seismic energy budgets, which questions landslide slip mechanisms, particularly the relationships between steady and transient aseismic creep and stick-slip. Furthermore, our understanding of the mechanisms of landslide slip is limited by two aspects: (1) stick-slip events have not yet been evidenced simultaneously on displacement data and seismic data in landslides; (2) transient creeps are most of the time observed on surface displacements, and very rarely directly on the sliding surface (Ruggeri et al., 2020). Therefore, the following questions about the origin of stick-slip events and creep bursts could be raised: Is seismicity linked to creep bursts? Is seismicity produced at the creeping surface or in the rock volume? What are the controlling factors of creep bursts? What is the link between the slip dynamics along a shear plane at the base of the landslide and the resulting surface motion?

To better quantify the mechanisms of the landslide sliding, the present study exploits the extensive instrumentation and long-term time series data of the Åknes landslide in Norway. Multi-methods measurements of different parameters such as displacement, seismicity, and groundwater pressure were acquired from 2012 to 2023. This landslide is instrumented at its surface with kinematic and seismic networks, and at depth with seven deep boreholes equipped with lines of inclinometers above, through and below the sliding basal plane, water pressure sensors, and a string of geophones. To detect and characterize creep bursts and establish their causal relationships, the present study investigates the unique data sets acquired on the Åknes landslide.

2 Geological setting

The Åknes landslide, located on the west coast of Norway along the Synnylvsfjorden fjord, was discovered by locals in 1964 (NGI, 1996). In the subsequent years, a few manual surface displacement measurement campaigns were conducted, followed by the installation of continuously recording surface extensometers. The landslide has been actively monitored since its discovery because of its potential to fail, which would cause a devastating tsunami that would impact nearby towns and the Geirangerfjorden fjord, a world heritage site selected by UNESCO in 2005.

The Åknes landslide is developing on a southeast-facing mountain with an average slope of 30-35° (Figure 1). An outcropping back scarp, approximately 30 m wide at its widest part to the west and a few meters wide to the east, is located 900 meters above sea level (masl). It forms the upper boundary of the landslide. The western and eastern borders include a sub-vertical strike-slip fault and shallow west-dipping faults. At two elevations along the slope, low-angle sliding surfaces outcrop and are parallel to the local foliation of the geological formations, with the lowermost sliding surface forming the lower boundary of the landslide at 150 masl. The landslide unstable area covers a surface area of 0.56 km^2 and contains an estimated volume of 54 million m^3 of rocks (Ganerød et al., 2008; Pless et al., 2021). The probability of landslide failure is divided into three scenarios, where the probability for each scenario is derived from a hazard score based on geologic structures and landslide slope activity (see Hermanns et al., 2013).

This landslide is located in the Western Gneiss Complex, consisting of orthogneiss ranging from mafic to granitic composition, but dominantly with granodioritic composition, with some places containing migmatites. The protolith age is between 1700 and 1600 Ma, and the rocks were metamorphosed during the Caledonian orogeny between 425 and 400 Ma (Corfu et al., 2014; Tveten, 1998). Core logs have revealed three lithological units comprising white to light grey granitic gneiss and pegmatite (62 vol.%), dark grey dioritic gneiss (23 vol.%), and black biotitic gneiss (15 vol.%). Locally, the gneiss contains biotite schist layers up to 20 cm thick (Ganerød et al., 2007; Ganerød, 2008; Langeland & Holmøy, 2018, 2019a, 2019b, 2019c; Sena & Braathen, 2021). The foliation is well-developed and folded around tight isoclinal folds plunging east-south-east (Braathen et al., 2004; Jaboyedoff et al., 2011). On outcrops, the dominating orientation of the foliation is parallel to the slope and dips at 30° on average. The dip angle of the foliation ranges from 27° to 34° in the core logs from the boreholes, which is inferred to be the range of different fold phases (Jaboyedoff et al., 2011; Kveldsvik et al., 2006). The sliding plane of the landslide and its back scarp follow the foliation and folds (Jaboyedoff et al., 2011). Drill cores show the shear zones are clay-rich and located mainly in biotite-rich gneiss, but some also consist of a mix of biotite-rich and granitic gneiss (Ganerød, 2008; Ganerød, 2013; Langeland & Holmøy, 2018, 2019a, 2019b, 2019c).

However, no correlation between lithology and fracture frequency was found by investigating the core logs from the latest drilling campaign (Papadimitrakis, 2020). The current interpretation is that the local stress state is the controlling factor, not the lithology (Pless et al., 2021).

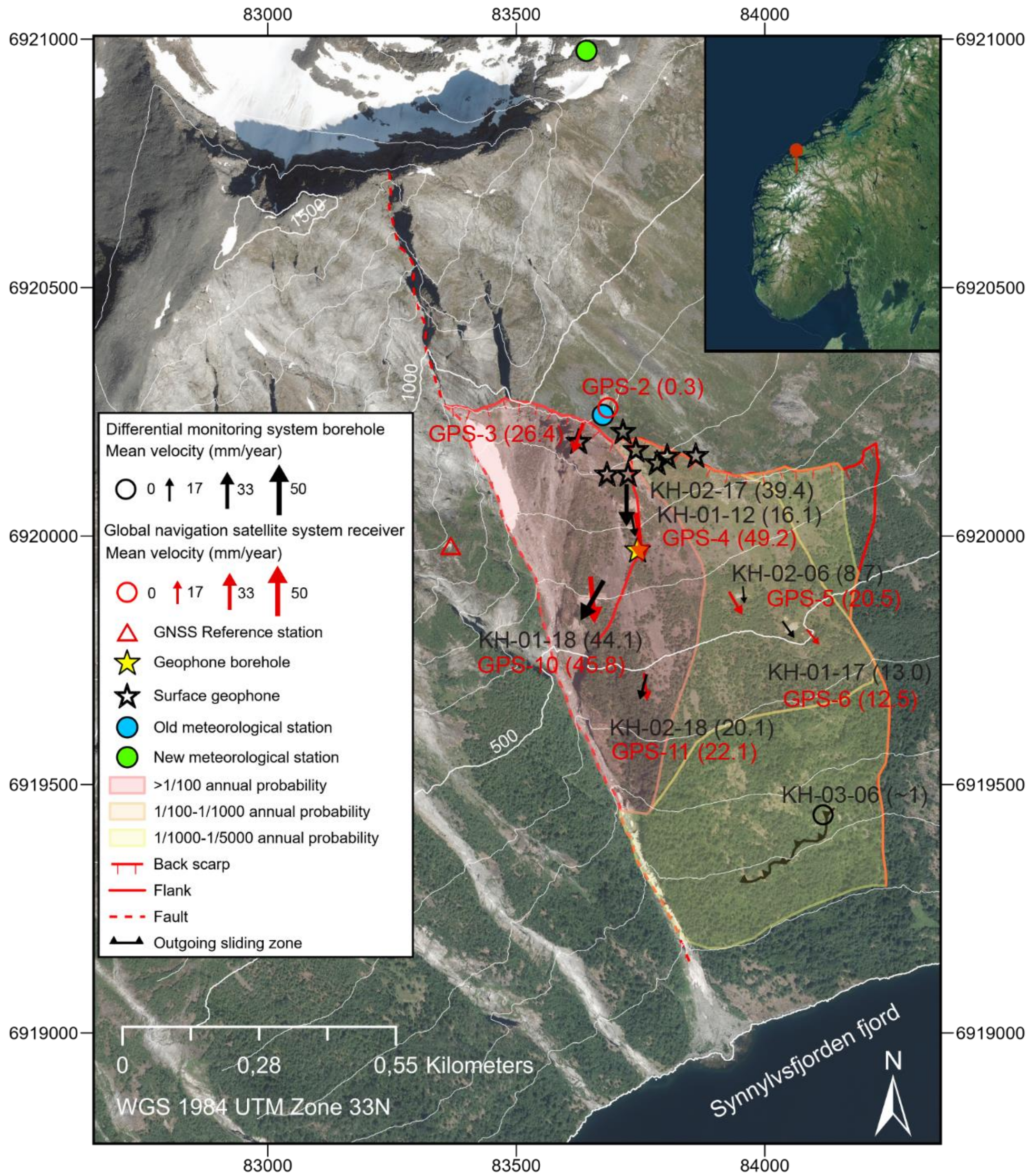

Figure 1. Map of the Åknes landslide with morphological structures, delineations of potential sliding scenarios and annual probability of a catastrophic collapse. Symbols indicate instrumentation where data from global navigation satellite systems (GPS, red arrows) and differential monitoring system boreholes (KH, black arrows) are displayed as mean velocity in mm/yr for the period 01/01/2020 to 28/03/2023. The length and width of arrows are proportional to the sliding velocity, which is also given as numbers in mm/yr in parenthesis on the figure. A circle is displayed if the instrument is nearly stable, with a velocity of less than 1 mm/yr. The sum of the shear zone sliding velocities is indicated for the boreholes where two shear zones

have been identified. The white lines are contours of equal elevations spaced every 100 m. The inset map shows the landslide location in Norway with a red marker.

3 Monitoring data, acquisition, and methods

The monitoring system for the Åknes landslide has been improved with the addition of instruments over many years. The data sets consist of a wide range of displacement, seismic, groundwater, and meteorological data densely covering the landslide's surface and at its sliding interface(s) at depth. The temporal resolution ranges from milliseconds to 1 hour, and the displacement resolution ranges from micrometres to millimetres. Data are transmitted automatically by radio link and optical fibre to be analyzed in near real-time for early warning purposes. Specifications on the type of sensors and acquisition parameters are given in Table 1. The location of the sensors is shown in Figure 1.

The instruments have been installed over two decades in an area prone to harsh weather conditions and practically only accessible by helicopter. The monitoring network is powered by a mix of solar panels and diesel generators installed in bunkers distributed on the landslide and away from it. The unstable slope is steep and prone to rock falls and snow avalanches that may damage both the sensors and their power cables. Power failure or damage to the instruments can take time to repair, explaining the gaps in the time series of some devices.

3.1 Surface displacement data

Ten Global Navigation Satellite Systems (GNSS) are distributed over the slope (Figure 1). We use relative positioning with one reference receiver on stable ground situated at 0.5 km from the landslide and post-processing on sequences of 12 hours of data to acquire displacement with millimetre precision ($\sigma = 0.6$ mm) as estimated by the company Cautus Geo who provided Trimble equipment and processed the time series of the GNSSs. Ice or snow on the antennas, may disturb the GNSS. We have removed a few outliers, i.e., sudden large spikes in the data, and filtered the time series of displacement by implementing a two-day median filter. The landslide surface velocity is calculated from the displacement time series by fitting a linear function over a given time window and ascribing the slope to the centre of that time window. For GNSS data, a linear fit over four days was chosen.

3.2 Borehole displacement and piezometric data

Twelve boreholes have been cored and logged, where seven of these are currently instrumented with a differential monitoring system (DMS) provided by the company Geoengineering Service Centre (CSG s.r.l) (Figures 1, 2). Three are DMS 2D Rock installations and four DMS 3D Multipacker installations that, in addition to the DMS 2D Rock, have several groundwater pressure sensors isolated by air-inflatable packers to monitor the water pressure in selected fracture zones. The depth of the boreholes ranges from 150 to 300 meters, well below the basal sliding surface of the landslide.

Both DMS 2D rock and DMS 3D Multipacker installations contain strings of inclinometers spaced one meter apart for approximately 150 meters. For the two newest DMS 3D Multipacker boreholes (KH-01-18 and KH-02-18), a few additional inclinometers are spaced more scarcely based on visual assessment of fracture zones from the core logs (Figure 2). Depending on the borehole location, each inclinometer string crosses one to two shear zones before entering the stable bedrock. The DMS 2D Rock is installed inside a plastic tube in the borehole, while the DMS 3D Multipacker is installed without a plastic tube and relies on air packers to keep the instrument centred in the borehole. Hourly sampling frequency is provided by both borehole types.

As the landslide moves along one or two shear zones, the DMS instrumentation line deforms over time and will eventually break in the future. We use data from six of the seven boreholes, as borehole KH-03-06, located on the Åknes slope below the active landslide zone, does not seem to have intersected a shear zone and does not record any displacement. The dataset is downloaded through the software DMS EW (CSG, 2005).

Two long time series are considered. The longest time series are recorded in boreholes KH-01-12 and KH-02-06 since late 2012. Four shorter time series have been acquired on boreholes KH-01-18 and KH-02-18 since late 2019 and boreholes KH-01-17 and KH-02-17 since late 2018 (Table 2). The dataset from the former two boreholes had noise caused by packer pressure changes, while the latter two boreholes suffered power issues several times. Consequently, the corresponding time series are set to start 01.01.2020.

3.2.1 Borehole displacement processing

In the boreholes, a shear zone deforms the line of inclinometers into an S-shape where the part below the shear plane is stable, and the part above it moves downhill (Figure 3). The actual displacement is given by cumulating the displacement recorded by one or more inclinometer modules inside the shear zone (Ruggeri et al., 2020).

For the DMS 3D Multipacker boreholes, the instrument string shows displacement created by inflation of the packers before a better inflation solution settled the problem. Therefore, we have removed this period in the time series. In addition to the inflation problems, a few electrical or technical errors on the borehole instruments have been solved by remotely resetting the modules and resetting the displacement to zero. We have detected these resetting events and raised the displacement to previous levels by adding the difference of a one-day median before and after the zero resets. We have removed a few outliers, i.e., sudden large spikes in the data, and filtered the time series by implementing a low pass filter of second order and a one-day cut-off frequency.

We calculated a time series of instantaneous velocity through a linear regression of the displacement time series with data every hour over one day, that is 24 data points per day. From this time series, we detect creep bursts through a short-time-average over long-time-average algorithm (STA/LTA), which has been developed to analyze seismic signals (Withers et al., 1998). The algorithm calculates the average value data on two successive time windows of differing durations and calculates the ratio or the difference between the two averages. Then, the user defines a threshold where the ratio or the difference is significant to detect a short-term event in the long-term time window.

We apply the STA/LTA algorithm to the velocity data calculated from the displacements measured in the shear plane of the landslide. Because the noise level varies in each borehole, we used different time windows for STA and LTA (Table 2), after a process of trial and errors. The LTA was set to 60 or 120 days, depending on the STA time window (Trnkoczy, 2012). Then, we calculated the difference d between the STA and LTA averages and defined the onset of a creep burst when d becomes larger than two times the standard deviation (σ^d). The end of each creep burst is defined when d decreases below one σ^d. The two standard deviation threshold enabled us to focus on fewer and larger events. The duration of the creep bursts depends on the choice of the values of STA and LTA. However, we have verified that the number and amplitude of the creep bursts detected do not vary significantly when these two values are slightly modified. Because of the high-quality displacement borehole data with a standard deviation of 0.02 mm, our STA/LTA algorithm can detect very small creep bursts with slip amplitude down to 0.1 mm.

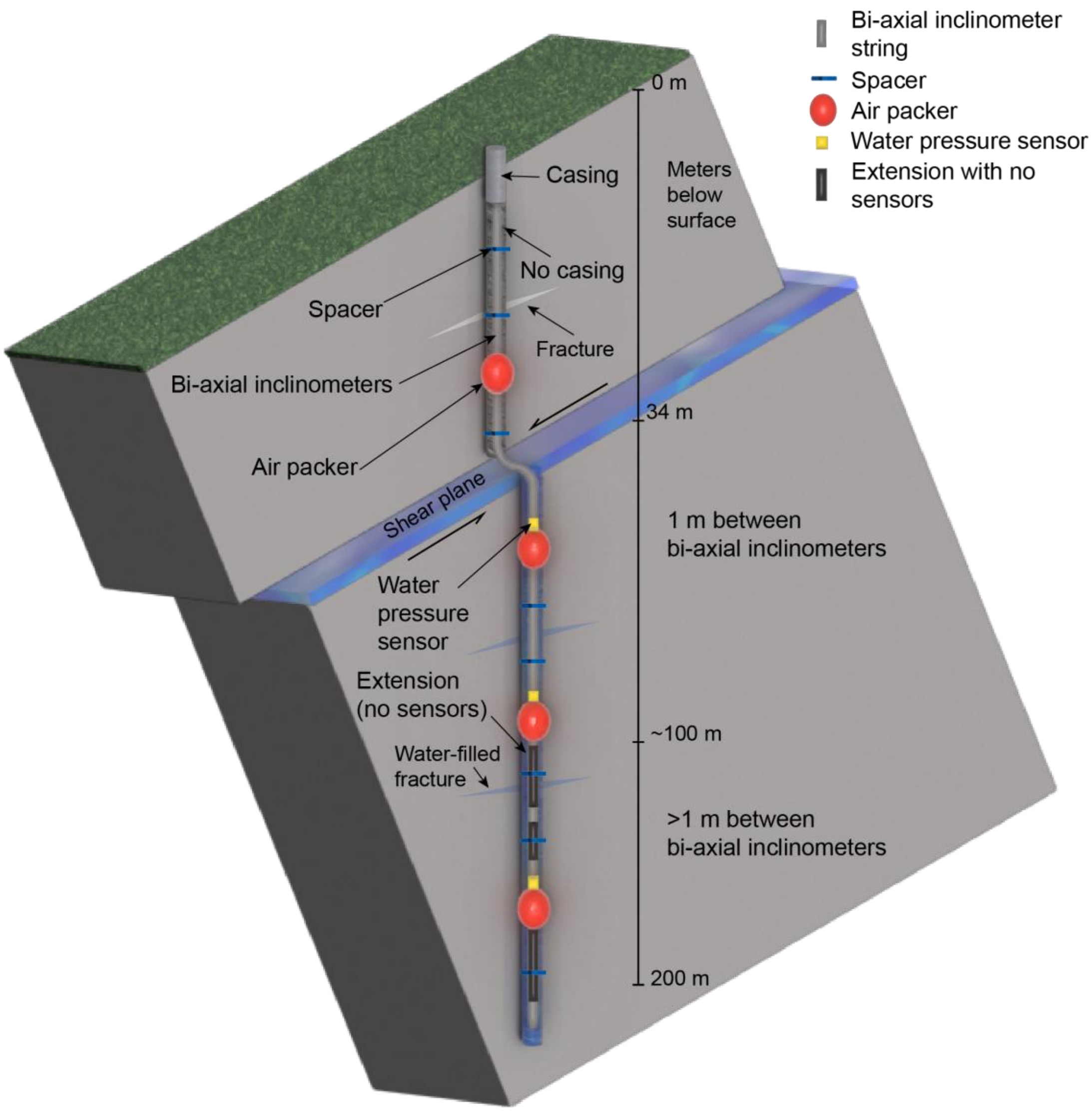

Figure 2. Sketch (not to scale) of the instrumentation in borehole KH-01-18, including the string of biaxial inclinometers, air packers, and water pressure sensors. This borehole crosses one shear plane in the landslide, along which the basal slip occurs, and continues in the bedrock below. The borehole contains 150 bi-axial sensors. Below the sliding zone, the borehole instrumentation contains segments without sensors along unfractured regions, and called extension joints, and segments with sensors that measure individual fractures identified in the core log. The sketch illustrates the use of biaxial inclinometers, air packers, and water pressure sensors to measure both displacement and water pressure in fracture zones and near other heterogeneities identified in the core log.

3.3 Surface geophone data

The Norwegian Seismic Array Institute (NORSAR) installed eight geophones at the surface close to the back scarp (black stars on Figure 1) starting from 2005 (Roth et al., 2006). The geophones are three-component short-period (4.5 Hz) sensors that record data with a 1000 Hz sampling rate and operate in trigger mode. They are connected to the acquisition system by long cables that, over the years, have been damaged by rock falls. Currently, four of the geophones are operative. A seismic catalogue from the surface geophone network is generated fully automatically and provides the time of the detected seismic events and their class (Langet & Silverberg, 2023). Detection times are helpful to compare and correlate the microseismic activity with other environmental parameters. Classes are essential to distinguish between seismic events directly associated with the landslide movement and other events (e.g., regional earthquakes, artificial noise, etc.). Additionally, the classes help differentiate between different types of events occurring on the landslide, as microseismic events could exhibit distinct waveforms depending on their mechanism (e.g., shear sliding or tensile opening). Here, seismic events related to the landslide's activity are classified into tremors, low-frequency earthquakes, and high-frequency earthquakes based on the characteristics of their signals (e.g., duration, frequency content and shape). The catalogue also includes other signals, such as rock falls, snow avalanches, and helicopter flights, that are removed in the present study.

3.4 Borehole geophone data

In 2017, NORSAR deployed a string of eight geophones in a borehole located in the most active part of the landslide (yellow star in Figure 1). The geophones are located between 15 and 50 m depth and equally spaced every 5 meters. They are three-component sensors, and data are recorded continuously with a sampling rate of 1000 Hz. Initially, the geophones were freely hanging on a string in the borehole. This free-hanging produced noise, a bias resolved in November 2021 by gluing plastic spacers around the geophone pods, thus enabling a good coupling with the borehole casing. Only borehole data after this date are considered here.

The borehole geophones catalogue is produced from a semi-automatic analysis of the data. While the detection is automatic, the event classification is performed manually by visually inspecting the waveforms. In the present study, only very high-frequency (100 to 400 Hz) and short-duration events (< 50 ms) are considered. These events likely occur very close to the borehole and are not detected by the surface geophones. Although the events cannot be located, their approximate depth can be inferred by using the depth of the geophone at which the first onset is detected, between 15 m and 50 m depth. This depth information is used further to compare the data to other time series.

3.5 Meteorological data

A meteorological station was installed in 2004 above the back scarp at 900 masl (blue circle on Figure 1). The location of this meteorological station is prone to severe weather events, resulting in periods of missing data. A new meteorological station has been installed at a more suitable location and has been operational since 2022 (green circle on Figure 1). For the meteorological parameters, we have downloaded data from seNorge (seNorge, 2023), a weather model service provided by the Norwegian Water Resources and Energy Directorate, the Norwegian Meteorological Institute, the Norwegian Public Road Administration, and the Norwegian Mapping Authority. We relied on this model due to missing data since 2021. The seNorge weather model uses input from all weather stations approved by the Norwegian Meteorological Institute and performs a statistical interpolation over a regular grid with grid spacing of 1 km, providing a time resolution of daily average values. The model is based on non-homogenized data, and after interpolation, the meteorological values are adjusted locally to fit better the observed data (Lussana, 2021). The seNorge model resembles the observed data from both the old and new meteorological stations where the standard deviations of the observed subtracted from modelled data for temperature are 1.97 ℃ (old station) and 2.09 ℃ (new station), and for precipitation, it is 3.17 mm (old station). The newest meteorological station does not yet transmit precipitation data due to sensor problems. However, it has good snow measurements, which the old station did not have, and the standard deviation of the observed subtracted from the modelled value of snow depth is 72 cm (measured in one season only).

Table 1. Table of instruments installed on the Åknes landslide by type, name, number of devices, installation date and operation period, acquisition frequency of the available data, and measurement resolution provided by the manufacturer.

Type	Product name	Number of instruments	Installation date(s)	Analysed period	Sampling frequency	Measurement resolution
GNSS	Trimble Net-R9 receivers with Trimble Zephyr 2 or 3 antennas	10	27/03/2007-03/10/2020	~12 years	1 second	<1 mm
Borehole inclinometers	CSG DMS 2D Rock	3	21/10/2007-22/08/2013	~11 years	1 hour	<0.3 mm
Borehole water pressure sensor						138 Pa
Borehole inclinometers	CSG DMS 3D Multipacker	4	29/08/2018-30/10/2019	~3 years	1 hour	<0.03 mm
Borehole water pressure sensors and air packers						138 Pa
Surface geophones	OYO GeoSpace GS-11D with Geometrics Geode digitiser	8	01/02/2007	~12 years	1000 Hz [4.5 Hz resonance frequency]	
Borehole geophones	OYO GeoSpace GS-14-L3 with Ref Tek 130 S01 digitizer	8 in one borehole	01/11/2017	~2 years	1000 Hz [24 Hz resonance frequency]	
Old meteorological station	Campbell SR50 - Snow depth	1	12/11/2004	~12 years	1 hour	0.25 mm
	Vaisala HMP45A - Temperature	1				0.2 ℃
	Geonor T-200B precipitation	1				0.1 mm
New meteorological station	Sommer USH-9 - Snow depth	1	19/10/2022	~1 year	1 hour	1 mm
	Sommer USH-9 - Temperature	1				0.1 ℃
	Vaisala WXT 530 - precipitation	1				0.1 mm

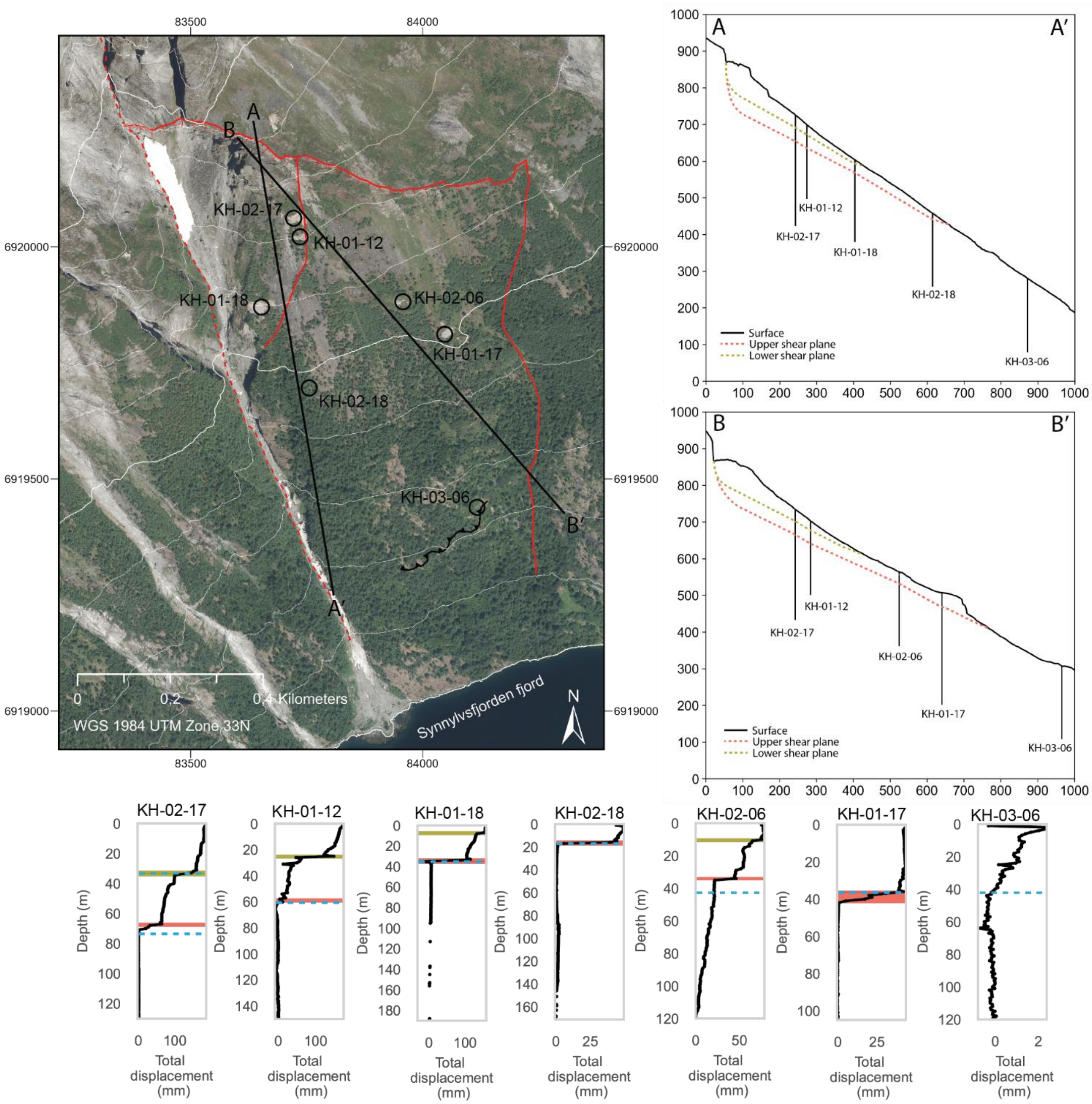

Figure 3. A conceptual model of the upper and lower shear zones identified in the boreholes installed on the Åknes landslide. The two profile lines with the respective boreholes are displayed on the map. The cumulated displacements measured in the boreholes display one or two distinct shear zones, except for borehole KH-03-06, where no active shear zone could be identified. On the plots, the y-axis is the depth below the landslide surface, and the x-axis shows the cumulated slip in each borehole for the period 01/01/2020-27/03/2023. The brown and pink lines on the plots indicate the upper and lower shear zone locations, while the blue dashed lines

indicate the mean groundwater level. On the 2D profiles, the shear zones where slip occurs are represented in brown and pink dashed lines.

Table 2. Period of detection, shear plane depth and shear zone material composition, parameters used for STA-LTA algorithm to detect creep bursts, number of detected creep bursts in each borehole, and total instrument depth. The shear plane column indicates boreholes with an upper and lower shear plane, while boreholes with one shear plane are left blank. The onset of creep burst detection is triggered when STA-LTA is above two standard deviations (2σ), and the end of each creep burst (de-trigger) is identified when STA-LTA is below one standard deviation (1σ).

Borehole	Period	Shear plane	Depth (m below ground)	Composition	Short term average (day)	Long term average (day)	Trigger	De-trigger	Number of creep bursts detected	Total depth of borehole instrument (m)
KH-02-06	02.07.2012 to 27.03.2023	Upper	8-9	Biotitic gneiss with 50 % content of biotite[a]	32	120	2□	1□	8	120
		Lower	33-34	Biotitic gneiss with 80 % content of biotite[a]					12	
KH-01-12	07.11.2012 to 27.03.2023	Upper	24-25	Granitic gneiss with varying biotite thickness[b]	12	60			11	150
		Lower	62-63	Dioritic gneiss with 2 cm thick clay layer on each side of 10 cm thick crushed rock[b]					10	
KH-01-17	15.11.2019 to 27.03.2023		35-41	Biotite-rich gneiss, clay and crushed rock 10 cm thick at 40 meters depth[c]	8				10	105
KH-02-17	15.10.2018 to 27.03.2023	Upper	30-34	Dioritic and biotite rich gneiss[d]	12				10	130
		Lower	66-70	Biotitic gneiss with clay and 30 cm crushed rock at 69 meters depth[d]					13	
KH-01-18	01.01.2020 to 27.03.2023		33-35	Dioritic and biotite-rich gneiss with clay and crushed rock 10 cm thick at 33 meters depth[e]	4				10	190
KH-02-18	01.01.2020 to 27.03.2023		14-17	Dioritic and biotite rich gneiss[f]	4				5	171

[a] Ganerød et al., 2007
[b] Ganerød, 2013
[c] Langeland & Holmøy, 2018
[d] Langeland & Holmøy, 2019b
[e] Langeland & Holmøy, 2019a
[f] Langeland & Holmøy, 2019c

4 Results

4.1 Long-term and seasonal displacements recorded at the surface and at depth

The displacement accumulated over all the line of inclinometers for the two 11-year long time series is 269.9 mm and 545.0 mm for boreholes KH-02-06 and KH-01-12, respectively. For the same period, the GNSSs at these locations (GPS-5 and GPS-4, see Figure 1) measured 307.6 mm and 556.5 mm of displacement, respectively.

The cumulative displacements in the four boreholes for the 3-year, shorter, time series range from 42.7 mm in borehole KH-01-17 to 186.22 mm in borehole KH-02-17, with a median value of 105.7 mm for all the boreholes. All boreholes move at different rates at the assumed shear planes (Figure 1). The six GNSS stations measuring displacement at the locations of the six boreholes for the same period range from 41.5 mm to 164.1 mm, with a median value of 72.3 mm. GPS 4 and GPS 10, and GPS 5 and GPS 11 are moving at a similar rate (~53 mm/yr and ~23 mm/yr). Along the shear planes in these boreholes, the displacements range from 1.2 mm in KH-01-12 lower shear zone to 146.2 mm in KH-01-18, with a median value of 42.2 mm. Boreholes KH-02-18 and KH-02-17 display similar displacement rates (~22 mm/yr) until the recording in borehole KH-02-18 ended in January 2022.

Four boreholes display two shear zones along the borehole column (Figure 3). In borehole KH-02-17, the upper- and lower-shear zones exhibit similar displacement rates (19.1 and 20.9 mm/year, respectively). The lower shear zone in borehole KH-02-06 has shown a consistent long-term rate of 4.7 mm/year, while the upper shear zone has increased its steady state creep over the past few years from 1.2 mm/year to 4.1 mm/year. For borehole KH-01-12, the lower shear plane dominated the displacement earlier, but this zone has been quiescent for the past three years. The movement has transitioned to the upper zone, increasing its displacement rate in the same period from 6.8 mm/year to 18.5 mm/year. A transition from the main shear zone in KH-01-18 to a new shear zone at 9 meters also started the last months of the analyzed dataset.

Surface displacements measured with GNSS display a seasonal pattern with one or two maximum velocities in early spring and late autumn to early winter and a minimum in summer (Figure 4). The shear zone displacements in the boreholes also display a seasonal pattern with two velocity peaks similar as the GNSS data. However, these patterns are not constant from year to year, except for GPS 6. The seasonal groundwater level recorded in open boreholes show a maximum in the autumn and a minimum in early summer. The long-term displacement rate in the boreholes is quite constant, but interrupted by creep bursts (Figure 5).

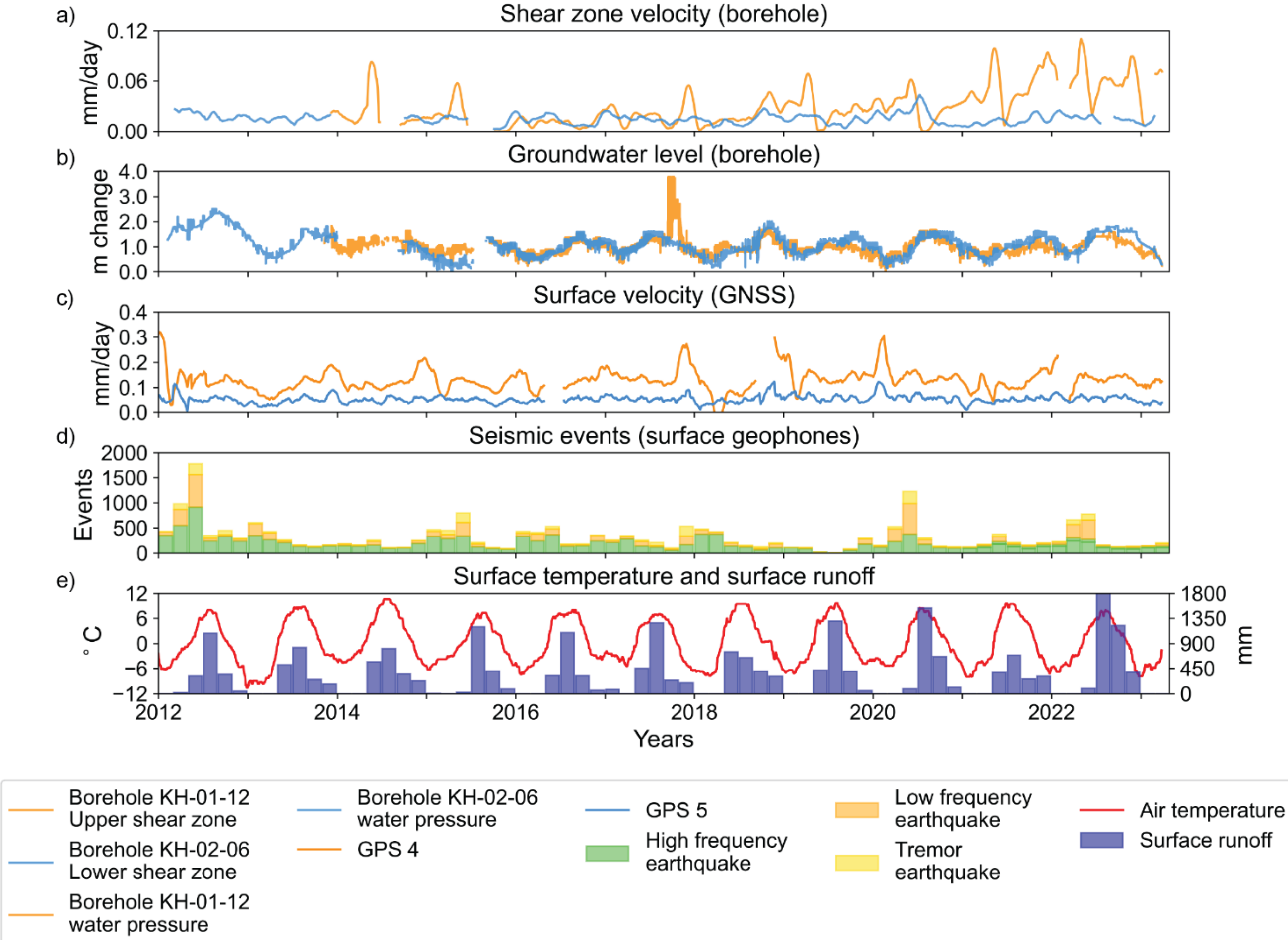

Figure 4. Time series recorded on the Åknes landslide in the period 01/01/2012-27/03/2023. (a) Shear plane slip velocities measured with inclinometers, (c) surface slip velocities measured with GNSS with two-week median filters and (b) groundwater levels with two-month median filter are displayed for boreholes KH-01-12 upper shear zone (blue curves) and KH-02-06 lower shear zone (orange curves). d) The surface geophones record seismic events. e) Air temperature (two-month median filter) and surface run-off (water equivalent of snowmelt and rain), see explanations in section 3.5. Seismic events and precipitations are summed over two-month periods.

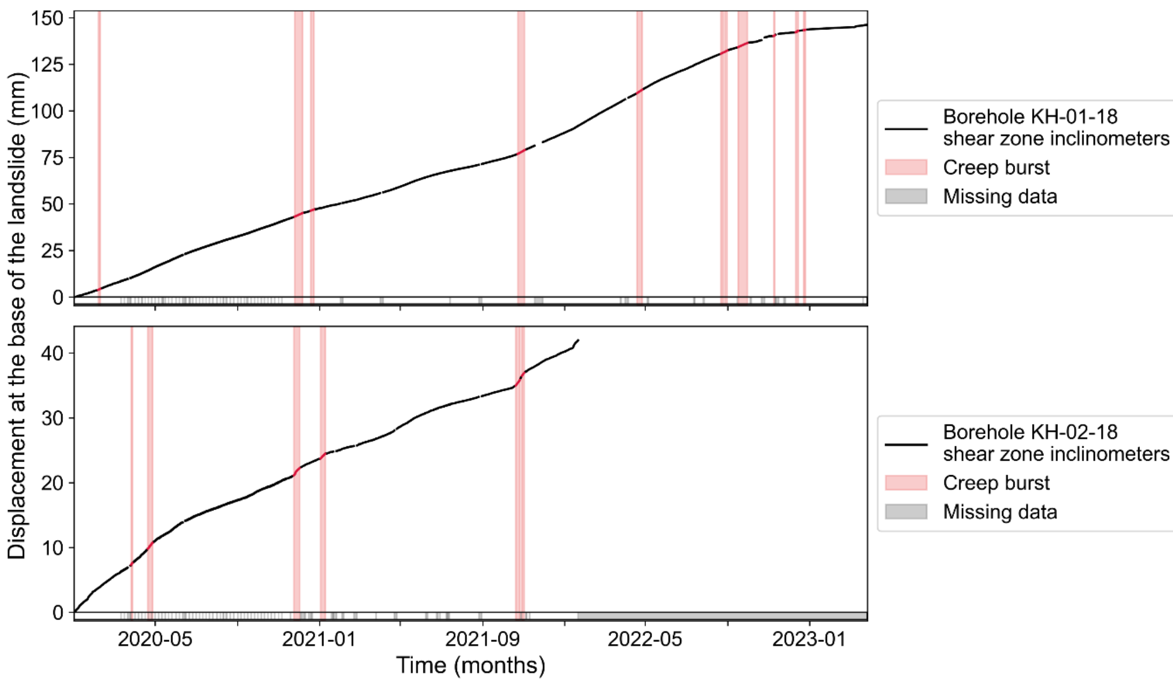

Figure 5. Time series of the displacements measured with inclinometers in boreholes KH-01-18 (upper panel) and KH-02-18 (lower panel), both located within the upper shear plane of the landslide. Periods of fairly steady-state sliding (black) alternate with eleven and six periods of accelerated velocity identified as creep bursts (pink), respectively. Periods with missing data are shown with horizontal grey bars. For these boreholes, creep bursts contribute to 7.9 % and 9.8 % of the total displacement over the periods 01/01/2020-28/03/2023 and 01/01/2020-20/01/2022, respectively.

4.2 Seasonal variations in water pressure and seismicity

The water pressure in most boreholes changes with the seasons (Figure 4). In the water pressure sensors, we generally observe that water pressure is higher in autumn and lower in spring. This effect is less visible in borehole KH-01-17, where the water pressure behaves atypically, and not as significant for boreholes KH-02-06 and KH-01-12, as these are open boreholes without air packers and would therefore display lower pressure amplitudes. We observe water pressure values indicating that the groundwater table is above the shear plane in boreholes KH-01-18 and KH-01-17 for the water pressure sensors isolated in the shear zones. The other boreholes show no water standing above the shear plane. For boreholes KH-02-17, KH-01-18 and KH-02-18, water pressure sensors located deeper than the shear plane display pressures above the elevation of the shear plane and for borehole KH-01-18, these values are up to 30 meters of water column above the shear plane (Figure S1). The groundwater pressure was stable in boreholes KH-02-06 and KH-02-18 and had a slightly decreasing trend in borehole KH-01-12 and the upper shear zone of borehole KH-01-18. A trend of 5 meter yearly decrease in water pressure was observed in the lower parts of borehole KH-01-18. Water pressure in boreholes KH-01-17 and KH-02-17 increased in the upper and lower shear zones, and a slight increase was observed in the year 2023 for borehole KH-03-06 (Table S1). The temperature measured at the depths of the water pressure sensors remained stable throughout the year. The water pressure sensor situated at 20 meters depth in borehole KH-02-18 is sufficiently close to the surface to be affected by surface temperature variations (Figure S2).

The air temperature has a median value of -0.3 °C. The maximum monthly average temperature ranges from 9 to 15 °C and the minimum from -5 to -2 °C. The yearly surface runoff ranged from 1250 mm in 2010 to 2889 mm in 2022, with a median value of 1734 mm/year. The timing and intensity of the surface runoff is also variable. However, most of the runoff is concentrated in early summer due to snow melt, where the monthly maximum ranged from 479 mm in 2014 to 894 mm in 2020.

The endogenic microseismicity from the surface geophone data displays a distinct seasonal pattern, with a maximum in the spring and a minimum in the autumn (Figure 4d). High-frequency events occur all year, while the proportion of low-frequency and tremor events increases in the spring.

The endogenic microseismicity from the borehole geophones displays a less distinct pattern, but generally, more events are detected in spring. The maximum activity for the measurement period is in January-February, the first year of the two-year time series. Events detected by the two uppermost geophones, at 20 m and 25 m depth, dominate the time series (Figure S3).

4.3 Creep bursts statistics

We detected 98 creep bursts in total over the 7 boreholes, with a median frequency of 2 creep burst events per year per borehole, ranging from 0.8 to 3.7 events per year (Table S2). The detected creep bursts occur throughout the year (Figures 5, 6, 7, and Table S2). Two periods of elevated creep burst activity occur in spring and autumn, where the latter is most prominent. The magnitude of slip during creep burst ranges from 0.1 mm to 3.4 mm (Figure 6), with a median value of 0.66 mm. These creep bursts contribute between 7.9 % and 23.6 % of the total slip along the shear zones of the landslide. When considering all the boreholes, the displacements during creep bursts contribute to a median value of 11 % of the total slip of the landslide.

In our catalogue of creep bursts, in each borehole strong positive correlations exist between total slip distance and duration ($r^2 > 0.7$), and moderate to strong correlation ($0.4 < r^2 < 0.7$) between maximum velocity and total slip distance, and maximum creep velocity and creep burst duration (Figure 6). For the latter two, no correlation ($r^2 < 0.2$) was observed in boreholes KH-01-18 and KH-02-18.

Most creep bursts are detected only in a single (73 %) or few boreholes (10 %). Only 17 % of the creep bursts are detected in all the boreholes (Figure 7). Boreholes KH-01-12 and KH-02-17 are located within 50 meters of each other but display quite different behaviours. Comparatively, borehole KH-01-12 shows large creep bursts, whereas borehole KH-02-17 has tiny ones (Figure 7). In the 3-year time series, the upper and lower shear zones of borehole KH-02-17 and the upper shear zone of borehole KH-01-12 show a similar total displacement in the range 60-66 mm.

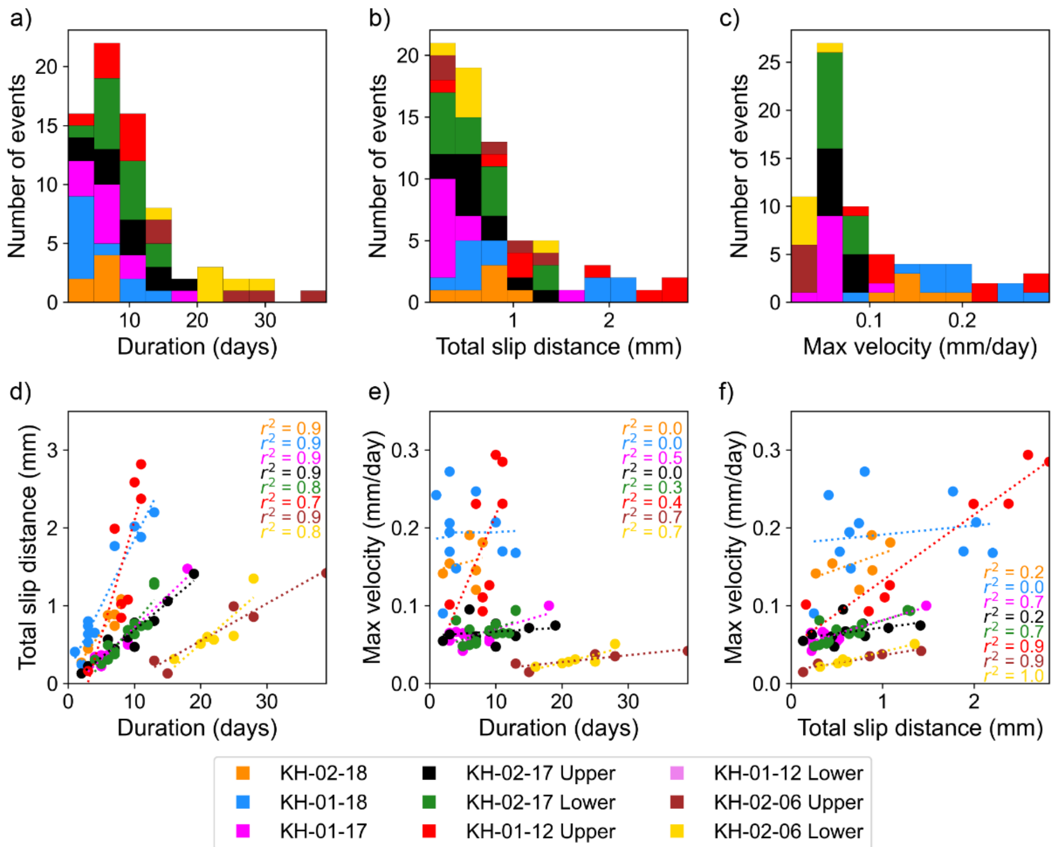

Figure 6. In six boreholes, all detected creep bursts in the 3-year time series (2020-2023). The plots display the distributions of creep bursts in relation to duration (a), total slip distance (b), and maximum slip velocity (c). In plots (d-f), each data point indicates a different creep burst. Total slip distance (d) and maximum velocity of creep burst (e) are plotted as a function of creep burst duration. The maximum slip velocity (f) is plotted as a function of the total slip distance. For boreholes that cross two active shear zones (Upper and Lower), creep bursts are indicated with different colours. Linear regression trends for each borehole and corresponding coefficients of determination (r^2) are displayed on the plots.

4.4 Correlation of creep bursts with groundwater pressure, meteorological parameters, and microseismicity

In order to assess the correlation of creep bursts with groundwater pressure, we looked at the water pressure sensor located in the shear zone of every borehole. When evaluating the effect of groundwater pressure on creep burst initiation, we observe a general relationship between creep bursts occurring at the seasonal high groundwater level in late autumn and at the seasonal low groundwater level in the spring (Figure 7). Looking closely at each creep burst, we often observe a local peak in water pressure preceding the onset of creep bursts occurring from autumn to spring (Table 3). This local peak is clearly observed in the water pressure sensors in the shear zone and not in the ones deeper below the shear zone. We do not observe these local peaks preceding creep bursts in the summer period.

Table 3. Summary of creep bursts per season with respective events correlated to a change in water pressure.

Season	% of events	% of events correlated to water pressure changes per season
Spring	23.5	34.8
Summer	15.3	6.7
Autumn	36.7	41.7
Winter	24.5	25.0

In spring, the groundwater level rises before creep bursts as a response to the infiltration of increased surface runoff derived from snowmelt. In autumn, groundwater level is influenced mainly by rainfall, and to a much lesser extent by snowmelt. Looking at the groundwater temperature change measured at the depth of the water pressure sensors, data do not show any change in temperature at the time of the creep bursts in any boreholes except one creep burst in KH-02-18. At this event, a drop in water temperature of 0.3 °C occurred at the water pressure spike during the snow melting season. These results show that the groundwater reaching the water pressure sensors at depth is clearly older than recent infiltration, as it has equilibrated to the local groundwater temperature.

We did not observe a systematic correlation between the seismic events from the surface geophones and creep bursts. However, we could observe a correlation between the largest creep burst recorded in multiple boreholes and above-average seismic activity in the borehole geophone data (Figure 8). The large majority of seismic events detected during this creep burst occurs at a depth around 25 meters, that is at the level of the shear zone at this location.

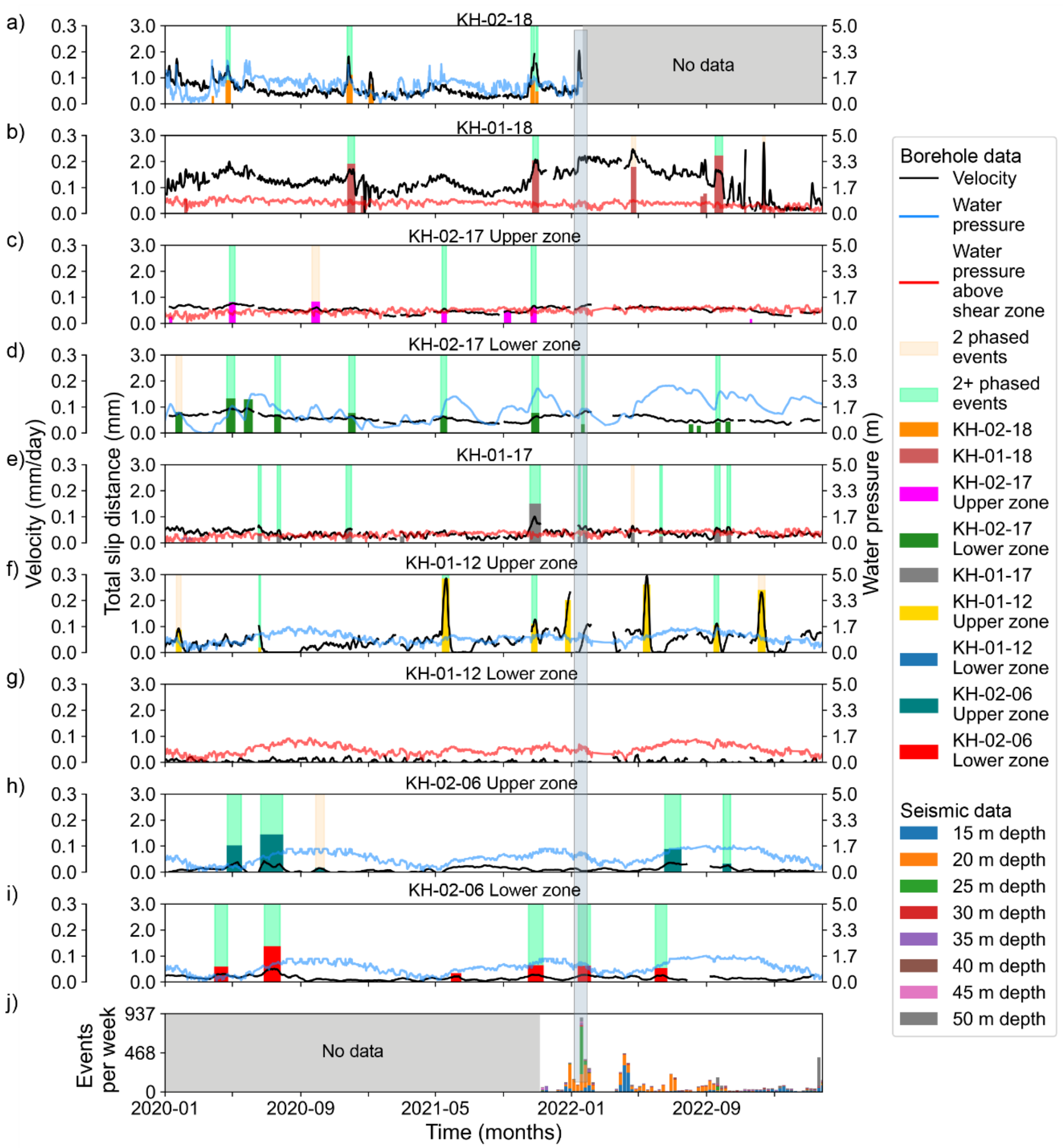

Figure 7. Time series of slip velocity (black curves) along the landslide shear zones at depth in five different boreholes. a-i) Slip velocity and water pressure in five boreholes. The water pressure is plotted in blue if the water table is located below the shear plane and in red if it is above. j) Weekly cumulated seismic events detected in the borehole geophone data. Boreholes KH-02-17, KH-01-12, and KH-02-06 cross two active shear zones, and data from these two zones are shown in separate panels. Creep bursts are shown as vertical bars whose lateral extent indicates their duration, and the vertical extent corresponds to the total displacement during the burst. Events seen on two boreholes are highlighted with transparent brown vertical rectangles, and those detected in more than two boreholes are highlighted with transparent green vertical rectangles. The other events are observed only in one borehole. Creep bursts occur throughout the year. However, events detected in several boreholes occur primarily in late autumn and

winter. The grey vertical bar extending over all panels highlights the creep burst plotted in Figure 8.

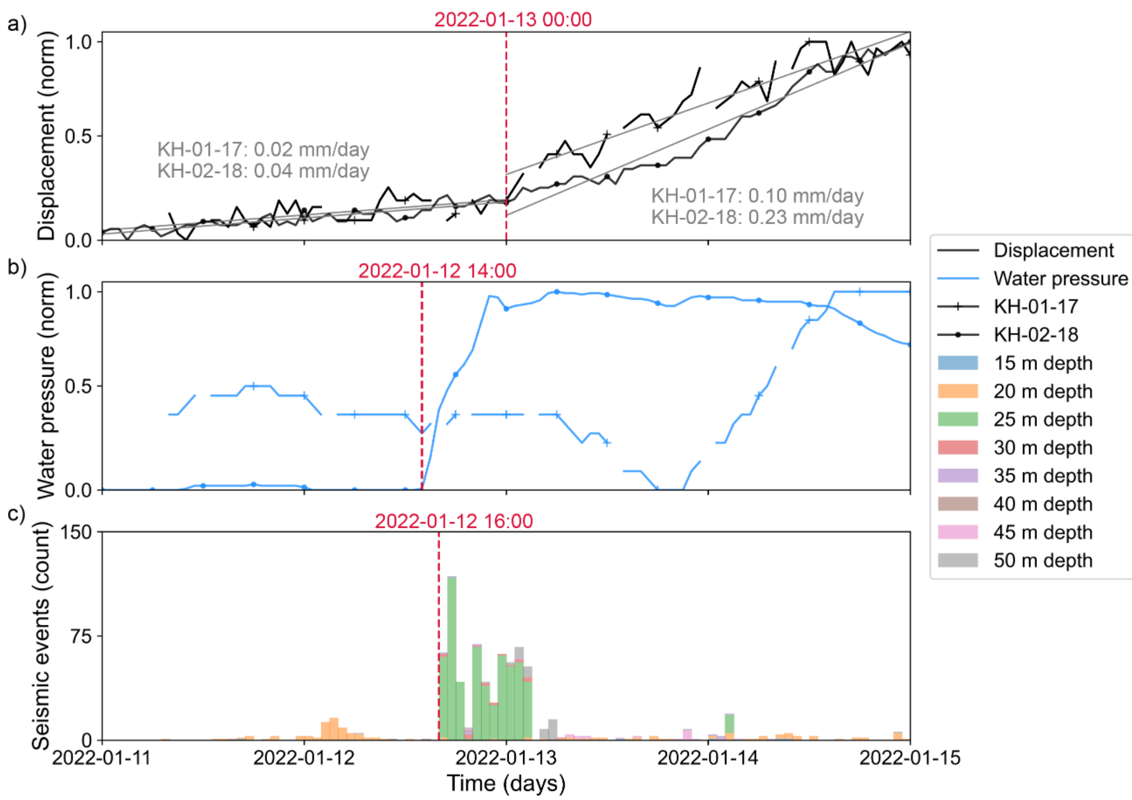

Figure 8. Zoom on the creep burst detected between the 12th and the 26th of January 2022, which was recorded in multiple boreholes (vertical grey bar in Figure 7). Here, we show the data of two boreholes where the amplitude of the signal is highest. a) Normalized borehole displacement measured by inclinometers in boreholes KH-01-17 and KH-02-18. Grey trend lines highlight changes in velocity between before and during the creep burst with their respective velocities. b) Normalized borehole water pressure. c) Seismic activity measured with borehole geophones. Data show an increase in groundwater pressure at the depth of the shear zone in one of the boreholes followed by an increase in seismic activity at a depth of 25 m, where the upper sliding plane is located. Then, the onset of creep burst occurred along the shear plane in the two boreholes. The vertical red dashed lines indicate the onset of an increase in each data set. The GNSS data is not displayed due to insufficient resolution to view the event. Data from all boreholes are shown in Figure S4.

5 Discussion

5.1 Seasonal displacements

The time series of inclinometers and GNSS displacement both display long-term motions with seasonal fluctuations. The Åknes landslide demonstrates a pattern of seasonal surface movement, reaching its highest velocity in late autumn and its lowest during summer. Meanwhile, the sub-surface displacement shows velocity peaks during both spring and autumn. This seasonal motion is related to snowmelt and precipitations and is associated with increased seismicity (Figure 4 and Table S2). The surface geophones display a distinct seasonal pattern of events, with a maximum in the spring and a minimum in the autumn. The high-frequency micro-seismic events are consistent throughout the year, while low-frequency and tremor seismic events increase in spring. Langet and Silverberg (2023) interpreted the high-frequency pattern as a constant signal from friction along the sliding plane, while the low-frequency and tremor events could correspond to fracturing events and water infiltration.

Previous studies on other landslides have shown a direct link between landslide velocity and groundwater pressure conditions forced by precipitations and snowmelt (e.g., Iverson & Major, 1992; Terzaghi, 1962). Two processes can be invoked: either a reduction of the normal stress due to pore-water variations at the level of the shear surface (e.g., Agliardi et al., 2020; Terzaghi, 1962) or enhanced rock degradation by water saturation of rocks (e.g., Atkinson, 1984; Voigtländer et al., 2018).

In the water pressure data of the Åknes landslide, we observe that all, except boreholes KH-01-18 and KH-01-17, display groundwater levels below the sliding zones. The water pressure sensor data show that the shear zones effectively drain excess water pressure. When looking below the shear zones, we see seasonal changes with high and low groundwater pressures in the autumn and spring, respectively. Sena and Braathen (2021) observed that the groundwater pressure fluctuated more in the upper part of the landslide than in the middle and lower parts, and the groundwater pressure trend increased for the upper part and was stable for the middle and lower parts of the landslide. With newer data, we found similar annual fluctuations ranging from two to four meters in the open boreholes. For the Multipacker boreholes, we observed fluctuations from 14 to 30 meters in water pressure sensors located below the shear zones and one to three meters in the shear zones. Groundwater pressure data analyzed now showed no relationship between decreasing trends and the altitude of the landslide surface. However, a large 5-meter annual decrease in water pressure was observed for the lower water pressure sensor in borehole KH-01-18 (Table S1).

Sena and Braathen (2021) modelled that ~90 % of groundwater recharge infiltrates into the back scarp that behaves as a groundwater reservoir. The seasonal groundwater fluctuations in the boreholes are the cumulative effect of a long recharge period, starting from early spring with snowmelt followed by rainfall throughout summer and autumn. If groundwater recharge would take place via relatively fast and vertical pathways near the boreholes, we would expect to observe a sharp decrease in groundwater temperature due to the infiltration of cold water during the snow-melting season. However, this is not evident in our measurements, corroborating a longer recharge period with a considerably higher infiltration in the back scarp (Figure S2). On the other hand, Frei (2008) measured the flow rate of springs from the outcropping sliding planes. The peak flow velocity of 17.4 m/h was very high compared to 30 m/h runoff measurements. These observations suggest that water infiltrates the back scarp, mixes and equilibrates its temperature before reaching the borehole sensors.

The surface runoff varies in timing and intensity during the measuring period. The wettest year was more than twice as wet as the driest year, and the month with the most intense surface runoff rate experienced double the intensity compared to the least intense month. We would expect an equivalent effect on the water pressure with higher peaks in the wetter years and months, but we did not detect such an effect in the boreholes. Previous studies indicate that there are likely many water pathways through fractures other than the two sliding planes and that these are interconnected at different locations, which could explain the highly variable behaviour of the different water pressure sensors (Frei, 2008; Sena & Braathen, 2021).

Yet, the seasonal water fluctuations align with the landslide's velocity changes, but the groundwater pressure variations recorded in the isolated shear zone appear insufficient to account for these velocity changes. Additionally, the water pressure sensors beneath the shear zone are hydraulically disconnected by air packers and are incapable of elucidating the fluctuations in landslide velocity. Thus, the water pressure measurements in the boreholes fail to explain the landslide velocity fluctuations by the conventional reduction of normal stress caused by elevated groundwater levels above the shear plane. This result aligns with numerical modelling studies showing that small water table increases above the sliding plane are insufficient to reduce the normal stress to promote sliding (Cancino & Lorig, 2020; Shabanimashcool & Kveldsvik, 2020).

In addition, changing inflow, outflow, and up-and-down-flow gradients of water pressure in the boreholes induce seepage forces along the slope, affecting the stability of the landslide (Elvebakk & Pless, 2018). Seepage forces change the direction of the total forces to pointing at some angle to the direction of flow rather than parallel to gravity (Mourgues & Cobbold, 2003). The heterogeneity of hydraulic diffusivity could also be important, as low diffusivity leads to destabilization and high creep rates that, at some point, fail to decelerate (Zhang et al., 2023). Using the Quiñones-Rozo (2010) method to estimate the hydraulic conductivity from the Lugeon tests conducted by the company Geodrilling (Langeland & Holmøy 2018, 2019a, 2019b, 2019c), we obtained low hydraulic conductivity (1×10^{-5} – 6×10^{-5} cm/s) for boreholes KH-01-18, KH-02-17 and KH-01-17, and medium hydraulic conductivity (2×10^{-4} – 6×10^{-4} cm/s) for borehole KH-02-18.

The higher creep rates of boreholes KH-01-18 and KH-02-17 corroborate Zhang et al. (2023) interpretation. Borehole KH-01-17 shows a lower creep rate than borehole KH-02-18, which has a much higher hydraulic conductivity but is also located in a slower-moving part of the landslide. Yet an alternative explanation to the seasonal velocity changes could be that the decreased strength of the rock is caused by stress corrosion due to seasonal water saturation, both by the changing groundwater levels and the infiltration from the surface (Atkinson, 1984; Cruden & Varnes, 1996), which can lead to higher water flow rates in the shear zones.

5.2 Creep bursts

The cumulated borehole displacement measured with inclinometers over the 11-year period (2012-2023) displays a similar magnitude and orientation to the surface displacement measured by GNSS. This is also the case for the 3-year period (2020-2023), except for borehole KH-01-12. This observation validates the inclinometer measurements and processing.

Despite this long-term consistency, the creep bursts are observed only in the inclinometer time series. We assume this is due (1) to the small magnitudes of the creep bursts (0.1-3.4 mm) in relation to the lower resolution of the GNSS measurements ($\sigma = 0.6$ mm) compared to the borehole inclinometers ($\sigma = 0.02$ mm), and (2) to the fact that the GNSS surface data measure an integrated dataset of the whole volume compared to the local measurements of the inclinometers. Therefore, relying solely on surface measurements would exclude important observations from the landslide's shear planes, especially when it deals with identifying when velocity changes occur.

Looking at the spatio-temporal distribution of creep bursts, 73 % are detected in a single borehole, 10 % in two boreholes, and 17 % in all boreholes. These observations suggest that the landslide shear zones contain some asperities that mostly slip individually but sometimes together. In addition, all boreholes move at different rates along the observed shear planes. This observation indicates that each borehole measures displacement at separate asperities inside the landslide. Until borehole KH-02-18 failed, it moved at a similar rate as borehole KH-02-17. This observation could indicate that those two asperities are underway to coalesce or already have. These observations give an idea of the asperity size, as the inter-distance between neighbouring boreholes in the landslide is between 50 to 150 meters, while the distance between KH-02-18 and KH-02-17 is 300 meters. The same assumption was made by Finnegan et al. (2022) by observing two extensometers separated by 100 meters that slipped independently. This observation and the observation of larger magnitude slips being geometrically limited by the asperities corroborated their hypothesis that larger-size asperities exhibited velocity-weakening properties.

In Åknes, creep bursts accommodate only 11% of the total displacement, while in Finnegan et al. (2022), most of the displacement was accommodated by creep bursts. There are differences in geology and instrumentation in these two study sites. The Oak Ridge earthflow consists of a rock mélange, compared to gneisses at the Åknes landslide, which is a less compliant rock. Also, the analyzed kinematic instrumentation consists of extensometers compared to borehole inclinometers at the depth of the sliding plane, respectively. The borehole instrumentation in Åknes provides information at the depth of the sliding plane that cannot be viewed from the surface, as already discussed above in this section. It could be that the magnitude of the creep bursts in the Åknes landslide is too small to be viewed from the surface with GNSS instruments of mm precision and that this is not true for the Oak Ridge landslide monitored with extensometers with 0.06 mm precision (Finnegan et al., 2022). In addition, the creep bursts are slipping for minutes at the Oak Ridge earthflow compared to days at the Åknes landslide. This difference might be attributed to the ten times faster displacement rate of the Oak Ridge earthflow.

5.3 Mechanisms of creep burst

At the Åknes landslide, we observe higher creep burst activity in spring and autumn, with most bursts occurring during autumn, corresponding to the groundwater low and high levels, respectively. Furthermore, the micro-seismic events in the borehole geophones display high-frequency events, i.e., the source is very close, with more events also in the spring and autumn, and the maximum occurring in January, in the first year of the time series (Figure S3). The record of the two geophones located closest to the surface at 15 and 20-meter depths dominated the total number of events. The sporadic events detected by the geophones at larger depths, i.e., 25 and 50 meters, are preceding creep bursts (Figure 8, S3, and S5). Consequently, we attribute these signals to the fracturing of small asperities along the shear plane. In addition to the creep bursts occurring at the seasonal groundwater high and low levels, we observe local groundwater level peaks before most creep bursts (Table 3). Water pressure magnitudes measured within the shear zones are insufficient to lift the landslide by fluid overpressure, i.e., buoyancy force. On the other hand, water pressure measured below the shear zones in boreholes KH-02-17 and KH-01-18 reaches water pressures above the shear planes. The water pressure recorded at the lowermost sensor in borehole KH-01-18 is as high as 30 meters above the sliding plane, and these changes exert frictional drag (i.e., seepage force) in the rock, adding to the driving forces. We would expect a relationship between seepage forces and slip velocity, but this effect is not visible in our dataset. Still, all creep bursts except in the summer seem to be related to groundwater level changes.

The increase in micro-seismicity at the shear zone depth less than one day before the largest creep burst event shown in Figure 8 also indicates a progressive damage process. Indeed, we have recorded two events where all boreholes slipped during the 3-year time series recorded in the geophone borehole (Figure 8, S4, and S5). In both instances, a spike of high-frequency microseismicity above the average was recorded at the depth of the shear plane (i.e., geophones located at 25 and 50 meters) a few hours before the creep burst. In Figure 8, we observe an increase in high-frequency events lasting eleven hours, where the second hour contained the highest rate of events. These events are not detected with the surface geophones, located approximately 200 m from the sub-surface geophones, showing their very small magnitudes. The principal acceleration of slip occurs at the end of the period with increased seismic events. This observation suggests that the creep burst nucleated following a phase of very small micro-quakes located at the level or near the shear zone. This behaviour mimics the behaviour of large earthquake nucleation (e.g., Bouchon et al., 2011).

Furthermore, for these two events, we also observe that water pressure increases before the seismicity by a few hours (Figures 8, S4 and S5). All these observations suggest that water flow increases stress corrosion (Atkinson 1984), due to the increased weathering and helps small fractures to develop. As a consequence, flaws within the landslide break due to progressive damage, forming narrow shear bands that coalesce into a primary failure plane with time and a sliding event occurs (Lacroix et al., 2013). This process can develop without large water level fluctuations above the shear planes, as for the Åknes landslide.

Finally, almost no seismic activity (neither from the surface nor from the subsurface geophones) occurred during the creep burst, showing that it is mostly aseismic. This shows that stick-slip is not the mechanism of these creep bursts.

5.4 Controlling factors of the creep bursts

Boreholes KH-02-17 and KH-01-12 are 50 meters apart on the same landslide unit (Figure 1) but display very different behaviours. In the last three years, borehole KH-02-17 measured a cumulated displacement twice larger than borehole KH-01-12. The lower shear zone in borehole KH-01-12 is quiescent, and the displacement in the upper shear zone follows a similar trend but with different rates for both boreholes. Also, the creep bursts in borehole KH-01-12 are about ten times larger than those in borehole KH-02-17. Local differences of lithological (Noda & Lapusta, 2013; Green & Moarone, 2002; Moore & Lockner, 2004) or geometrical (Jolivet et al., 2015) properties near these two boreholes could explain a significant contrast of friction over such a small distance. Indeed, the cored shear zones of KH-02-17 and KH-01-12 differ by comprising biotitic gneiss with a 30 cm thick clay layer compared to dioritic gneiss with a 2 cm clay layer (Table 2). This observation may explain the smaller creep bursts recorded in borehole KH-02-17 by a rate-strengthening behaviour and the larger creep bursts recorded in borehole KH-01-12 by a rate-weakening behaviour. Also, the slip velocity of the upper shear zone in borehole KH-01-12 increased while it decreased in the lower shear zone, which could be explained by an interaction between the displacement patterns observed at the shear zones that cross the two boreholes. As the uppermost borehole (KH-02-17) moves more than the lower one (KH-01-12), some stress must accumulate between them (Cruden & Varnes, 1996), increasing the shear stress at borehole KH-01-12. This effect could explain the larger slips measured in borehole KH-01-12 compared to borehole KH-02-17, which displays a steadier creep displacement.

Another interesting development is the current slow-down of slip recorded in borehole KH-01-18 (Figure 5), which was previously (2020-2023) the fastest-moving borehole. This borehole displayed an up-flow of 2400 l/h in a flowmeter test (Elvebakk & Pless, 2018) and has shown groundwater levels up to the shear plane for all water pressure sensors (Figure S1). The lowermost water pressure sensors display a downward water level trend of 5 m per year since 2020. This is exceptionally high compared to the other boreholes (Table S1).

This lowering of the groundwater level may explain the change in the borehole's displacement rate by lowering the amount of available water and, consequently, stress corrosion. However, no such trends are observed in the water sensors close to the shear plane, and there is no indication that the water pressure in the shear zone is affected by water pressure fluctuations registered deeper down in this borehole.

Wei et al. (2013) suggested that lithological heterogeneities may control frictional properties that are affected by the thickness of the shear zone and the imposed stress. All shear zones contain some weak clay layers where the rock type mainly comprises biotite-rich gneiss, with some also consisting of a mix of biotite-rich and granitic gneiss (Ganerød, 2013; Ganerød et al., 2008; Langeland & Holmøy, 2018, 2019a, 2019b, 2019c). This heterogeneous composition of the rock will result in different frictional properties, but more so, differences in shear zone thickness, which might help explain why boreholes KH-01-18 and KH-02-18 display higher displacement rates, as they exhibit comparatively narrow shear zones.

The question of how and if water pressure far below the shear plane affects the stability of a landslide remains unanswered. A potential explanation may be that the deeper zones with high water pressure are connected to the shear zone through fractures, making their fluctuations affect the flow rate in the shear zone.

6 Conclusions

Creep bursts are key expressions of landslide, tectonic fault or glacier stability. Their mechanics remain unclear due to their small magnitudes and the difficulty of only detecting and studying them from observations at the surface. Here, we utilize the extensive dataset on the Åknes landslide, Norway, that provides a unique opportunity to study the landslide's mechanics by comparing the shear zone's local dynamics, measured in a series of boreholes, and the resulting displacement at the surface. We detect creep bursts at the depth of the shear planes and analyze them regarding the surface motion. We also analyze water pressure and seismic data to correlate them to the creep burst mechanism. We measured that creep bursts accommodate 11 % of the total displacement of the Åknes landslide. The GNSS surface displacement is analogous to the entire borehole's cumulated displacement but cannot resolve the detected creep bursts by the borehole inclinometers along the shear plane. Most creep bursts occurred in separate locations and times, but when all boreholes slipped at once, we measured a correlation between water pressure rise before the creep burst and an increasing microseismic activity at the depth of the shear plane shortly after, followed by a transient acceleration. These observations indicate that creep bursts result from a degradation process in the landslide shear basal plane rather than an expression of a stick-slip mechanism, as the former would cause microseismic activity during the event. Even with such an extensive dataset, it is, however, difficult to pinpoint the cause of these events, except for the largest ones that are related to groundwater pressure variations. The smallest creep events occur without water pressure changes at the initiation of the motion. The creep velocity variations associated with water level changes could be attributed to increased rock degradation caused by stress corrosion from higher water flow rates in the shear plane. Measuring the flow rate in the shear planes in the future could help test this hypothesis, along with a more extensive analysis of microseismic data.

Acknowledgments

The Norwegian Water Resources and Energy Directorate (NVE) and the University of Oslo (UiO) funded this work. We thank Mario Lovisolo and Enza Garbarino at CSG for technical support. FR acknowledges support from the project FricFrac funded by the Center for Advanced Study (CAS) at the Norwegian Academy of Science and Letters during the academic year 2023-2024. We thank Ioannis Papadimitrakis, Fabian Barras, Einat Aharonov, and Mario Lovisolo for helpful discussions.

Open Research

The time series data of the Åknes landslide are available with a Digital Object Identifier (doi) number (Aspaas, 2024).

References

Agliardi, F., Scuderi, M. M., Fusi, N., & Collettini, C. (2020). Slow-to-fast transition of giant creeping rockslides modulated by undrained loading in basal shear zones. *Nature Communications*, *11*(1), 1-11. https://doi.org/10.1038/s41467-020-15093-3

Aspaas, A. (2024). Time series Aknes landslide, Norway [Data set]. Norstore. https://doi.org/10.11582/2024.00036

Atkinson, B. K. (1984). Subcritical crack growth in geological materials. *Journal of Geophysical Research: Solid Earth, 89*(B6), 4077-4114. https://doi.org/10.1029/JB089iB06p04077

Braathen, A., Blikra, L. H., Berg, S. S., & Karlsen, F. (2004). Rock-slope failures in Norway; type, geometry, deformation mechanisms and stability. *Norwegian Journal of Geology*, *84*(1), 67-88.

Brideau, M. A., Yan, M., & Stead, D. (2009). The role of tectonic damage and brittle rock fracture in the development of large rock slope failures. *Geomorphology*, *103*(1), 30-49. http://dx.doi.org/10.1016/j.geomorph.2008.04.010

Bouchon, M., Karabulut, H., Aktar, M., Özalaybey, S., Schmittbuhl, J., & Bouin, M. P. (2011). Extended nucleation of the 1999 M w 7.6 Izmit earthquake. S*cience, 331*(6019), 877-880. https://doi.org/10.1126/science.1197341

Cancino, C., & Lorig, L. (2020). *Geomechanical Modeling for Åknes Landslide*. Retrieved from https://publikasjoner.nve.no/eksternrapport/2024/eksternrapport2024_05.pdf

Corfu, F., Andersen, T., & Gasser, D. (2014). The Scandinavian Caledonides: main features, conceptual advances and critical questions. *Geological Society, London, Special Publications, 390*(1), 9-43. http://dx.doi.org/10.1144/SP390.25

Cruden, D., & Varnes, D. (1996). *Landslide types and processes*. Landslides, Investigation and Mitigation, ed. AK Turner and RL Schuster. Transportation Research Board, Special Report, 247, 36475.

CSG (2007). DMS EW (Version 4.9.21.9.): Centro Servizi de Geoingegneria (CSG) [software]. Retrieved from https://www.csgsrl.eu/eng/dms-software.html

Dille, A., Kervyn, F., Bibentyo, T. M., Delvaux, D., Ganza, G. B., Mawe, G. I., Buzera, C. K., Nakito, E. S., Moeyersons, J., Monsieurs, E., Nzolang, C., Smets, B., Kervyn, M., & Dewitte, O. (2019). Causes and triggers of deep-seated hillslope instability in the tropics–Insights from a 60-year record of Ikoma landslide (DR Congo). *Geomorphology*, *345*, 106835. https://doi.org/10.1016/j.geomorph.2019.106835

Elvebakk, H., & Pless, G. (2018). *Borehullslogging Åknes, Stranda kommune, 2017 – 2018*. Retrieved from https://www.ngu.no/publikasjon/borehullslogging-aknes-stranda-kommune-2017-2018

Finnegan, N., Brodsky, E., Savage, H., Nereson, A., & Murphy, C. (2022). Seasonal Slow Landslide Displacement Is Accommodated by mm-Scale Stick-Slip Events. *Geophysical Research Letters, 49*(20), e2022GL099548. https://doi.org/10.1029/2022GL099548

Frei, C. (2008). Groundwater flow at the Åknes rockslide site (Norway): Results of a multi-tracer test, (Master thesis).

Ganerød, G. V., Grøneng, G., Aardal, I. B., & Kveldsvik, V. (2007). *Logging of drill cores from seven boreholes at Åknes, Stranda municipality, Møre and Romsdal County*. Retrieved from https://www.ngu.no/publikasjon/logging-drill-cores-seven-boreholes-aknes-stranda-municipality-more-og-romsdal

Ganerød, G. V. (2008). *Structural mapping of the Åknes Rockslide, Møre and Romsdal County, Western Norway. NGU Report nr. 42*. Retrieved from https://hdl.handle.net/11250/2664622

Ganerød, G. V., Grøneng, G., Rønning, J. S., Dalsegg, E., Elvebakk, H., Tønnesen, J. F., Kveldsvik, V., Eiken, T., Blikra, L. H., & Braathen, A. (2008). Geological model of the Åknes rockslide, western Norway. *Engineering Geology, 102*(1-2), 1-18. https://doi.org/10.1016/j.enggeo.2008.01.018

Ganerød, G. V. (2013). *Geological logging of drill cores from borehole KH-08-12 at Åknes, Møre and Romsdal, Western Norway*. Retrieved from https://www.ngu.no/publikasjon/geological-logging-drill-cores-borehole-kh-08-12-aknes-more-og-romsdal-western-norway

Gomberg, J., Schulz, W., Bodin, P., & Kean, J. (2011). Seismic and geodetic signatures of fault slip at the Slumgullion Landslide Natural Laboratory. *Journal of Geophysical Research: Solid Earth*, *116*(B9). https://doi.org/10.1029/2011JB008304

Green, H. W., & Marone, C. (2002). Instability of deformation. *Reviews in mineralogy and geochemistry*, *51*(1), 181-199. http://dx.doi.org/10.2138/gsrmg.51.1.181

Gudmundsson, A. (2016). The mechanics of large volcanic eruptions. *Earth-Science Reviews*, *163*, 72-93. https://doi.org/10.1016/j.earscirev.2016.10.003

Helmstetter, A., & Garambois, S. (2010). Seismic monitoring of Séchilienne rockslide (French Alps): Analysis of seismic signals and their correlation with rainfalls. *Journal of Geophysical Research: Earth Surface*, *115*(F3). https://doi.org/10.1029/2009JF001532

Hermanns, R., Oppikofer, T., Anda, E., Blikra, L. H., Böhme, M., Bunkholt, H., Crosta, G., Dahle, H., Devioli, G., Fischer, L., Jaboyedoff, M., Loew, S., Sætre, S., & Yugsi Molina, F. X. (2013). Hazard and risk classification for large unstable rock slopes in Norway. *Italian Journal of Engineering Geology and Environment*, *2013*(TOPIC2), 245-254. https://dx.doi.org/10.4408/IJEGE.2013-06.B-22

Iverson, R. M., & Major, J. J. (1987). Rainfall, ground-water flow, and seasonal movement at Minor Creek landslide, northwestern California: Physical interpretation of empirical relations. *Geological Society of America Bulletin*, *99*(4), 579-594. https://doi.org/10.1130/0016-7606(1987)99%3C579:RGFASM%3E2.0.CO;2

Iverson, R. M. (2005). Regulation of landslide motion by dilatancy and pore pressure feedback. *Journal of Geophysical Research: Earth Surface*, *110* (F02015). https://doi.org/10.1029/2004JF000268

Jaboyedoff, M., Oppikofer, T., Derron, M.-H., Blikra, L. H., Böhme, M., & Saintot, A. (2011). Complex landslide behaviour and structural control: a three-dimensional conceptual model of Åknes rockslide, Norway. *Geological Society, London, Special Publications*, *351*(1), 147-161. http://dx.doi.org/10.1144/SP351.8

Jolivet, R., Candela, T., Lasserre, C., Renard, F., Klinger, Y., & Doin, M. P. (2015). The burst-like behavior of aseismic slip on a rough fault: The creeping section of the Haiyuan fault, China. *Bulletin of the Seismological Society of America*, *105*(1), 480-488. http://dx.doi.org/10.1785/0120140237

Jolivet, R., Jara, J., Dalaison, M., Rouet-Leduc, B., Özdemir, A., Dogan, U., Çakir, Z., Ergintav, S., & Dubernet, P. (2023). Daily to Centennial Behavior of Aseismic Slip Along the Central Section of the North Anatolian Fault. *Journal of Geophysical Research: Solid Earth*, *128*(7), e2022JB026018. https://doi.org/10.1029/2022JB026018

Kilburn, C. R., & Petley, D. N. (2003). Forecasting giant, catastrophic slope collapse: lessons from Vajont, Northern Italy. Geomorphology, 54(1-2), 21-32. http://dx.doi.org/10.1016/S0169-555X(03)00052-7

Kveldsvik, V., Eiken, T., Ganerød, G. V., Grøneng, G., & Ragvin, N. (2006, April). Evaluation of movement data and ground conditions for the Åknes rock slide. *International Symposium on Stability of Rock Slopes in Open Pit Mining and Civil Engineering Situations,* 3, 279-299.

Lacroix, P., & Amitrano, D. (2013). Long-term dynamics of rockslides and damage propagation inferred from mechanical modeling. *Journal of Geophysical Research: Earth Surface*, *118*(4), 2292-2307. https://doi.org/10.1002/2013JF002766

Lacroix, P., Handwerger, A. L., & Bièvre, G. (2020). Life and death of slow-moving landslides. *Nature Reviews Earth & Environment*, *1*(8), 404-419. https://doi.org/10.1038/s43017-020-0072-8

Lacroix, P., Belart, J. M., Berthier, E., Sæmundsson, Þ., & Jónsdóttir, K. (2022). Mechanisms of landslide destabilization induced by glacier-retreat on Tungnakvíslarjökull area, Iceland. *Geophysical Research Letters, 49*(14), e2022GL098302. https://doi.org/10.1029/2022GL098302

Lacroix, P., & Helmstetter, A. (2011). Location of seismic signals associated with microearthquakes and rockfalls on the Séchilienne landslide, French Alps. *Bulletin of the Seismological Society of America*, *101*(1), 341-353. https://doi.org/10.1785/0120100110

Langeland, H., & Holmøy, K. H. (2018). *Data report core logging KH-01-17*. Retrieved from https://hdl.handle.net/11250/3105277

Langeland, H., & Holmøy, K. H. (2019a). *Data report core logging KH-01-18*. Retrieved from https://hdl.handle.net/11250/3105288

Langeland, H., & Holmøy, K. H. (2019b). *Data report core logging KH-02-17*. Retrieved from https://hdl.handle.net/11250/3105287

Langeland, H., & Holmøy, K. H. (2019c). *Data report core logging KH-02-18*. Retrieved from https://hdl.handle.net/11250/3105289

Langet, N., & Silverberg, F. M. J. (2023). Automated classification of seismic signals recorded on the Åknes rock slope, Western Norway, using a convolutional neural network. *Earth Surface Dynamics, 11*(1), 89-115. https://doi.org/10.5194/esurf-11-89-2023

Lay, T., & Nishenko, S. P. (2022). Updated concepts of seismic gaps and asperities to assess great earthquake hazard along South America. *Proceedings of the National Academy of Sciences*, *119*(51), e2216843119. https://doi.org/10.1073/pnas.2216843119

Lussana, C. (2021). *seNorge observational gridded dataset. seNorge_2018, versions 21.09 and 21.10*. MET report, Report 07/2021. Retrieved from http://dx.doi.org/10.13140/RG.2.2.36336.38400

Mainsant, G., Larose, E., Brönnimann, C., Jongmans, D., Michoud, C., & Jaboyedoff, M. (2012). Ambient seismic noise monitoring of a clay landslide: Toward failure prediction. Journal of Geophysical Research: Earth Surface, 117(F01030). https://doi.org/10.1029/2011JF002159

Moore, D. E., & Lockner, D. A. (2004). Crystallographic controls on the frictional behavior of dry and water-saturated sheet structure minerals. *Journal of Geophysical Research: Solid Earth, 109*(B03401). https://doi.org/10.1029/2003JB002582

Mourgues, R., & Cobbold, P. (2003). Some tectonic consequences of fluid overpressures and seepage forces as demonstrated by sandbox modelling. Tectonophysics, 376(1-2), 75-97. http://dx.doi.org/10.1016/S0040-1951(03)00348-2

NGI, 1996. Åkernes Landslide - General Description of the Åkernes Slide Area and Control Measures. 585910-9, Norwegian Geotechnical Institute, Oslo.

Noda, H., & Lapusta, N. (2013). Stable creeping fault segments can become destructive as a result of dynamic weakening. *Nature, 493*(7433), 518-521. https://doi.org/10.1038/nature11703

Papadimitrakis, I. (2020). *Åknes rock mass characterization, Januray-July 2020.* Internal report, UiO NVE collaboration project. Retrieved from https://publikasjoner.nve.no/eksternrapport/2024/eksternrapport2024_09.pdf

Pless, G., Blikra, L. H., & Kristensen, L. (2021). *Possibility for using drainage as mitigation to increase the stability of the Åknes rock-slope instability, Stranda in western Norway,* NVE Rapport nr. 22. Retrieved from https://publikasjoner.nve.no/rapport/2021/rapport2021_22.pdf

Poli, P. (2017). Creep and slip: Seismic precursors to the Nuugaatsiaq landslide (Greenland). Geophysical Research Letters, 44(17), 8832-8836. https://doi.org/10.1002/2017GL075039

Quiñones-Rozo, C. (2010). *Lugeon test interpretation, revisited*. Paper presented at the Collaborative management of integrated watersheds, US Society of Dams, 30th annual conference. Retrieved from https://silo.tips/download/lugeon-test-interpretation-revisited-camilo-quiones-rozo-pe-1-abstract

Roth, M., Dietrich, M., Blikra, L. H., & Lecomte, I. (2006). Seismic monitoring of the unstable rock slope site at Åknes, Norway. In *Symposium on the Application of Geophysics to Engineering and Environmental Problems 2006* (pp. 184-192). Society of Exploration Geophysicists. http://dx.doi.org/10.4133/1.2923645

Ruggeri, P., Fruzzetti, V. M., Ferretti, A., & Scarpelli, G. (2020). Seismic and rainfall induced displacements of an existing landslide: findings from the continuous monitoring. *Geosciences, 10*(3), 90. https://doi.org/10.3390/geosciences10030090

Sena, C., & Braathen, A. (2021). *Åknes rock-slope failure hydrogeology: final report*. Retrieved from https://publikasjoner.nve.no/eksternrapport/2024/eksternrapport2024_09.pdf

seNorge. (2023). Varsom seNorge [Dataset]. Retrieved from https://www.senorge.no/

Shabanimashcool, M., & Kveldsvik, V. (2020). *Drainage Åknes - Coupled hydro-mechanical stability analysis of Åknes rock slope*. Retrieved from https://hdl.handle.net/11250/3105292

Templeton, D. C., Nadeau, R. M., & Bürgmann, R. (2008). Behavior of repeating earthquake sequences in central California and the implications for subsurface fault creep. *Bulletin of the Seismological Society of America*, *98*(1), 52-65. https://doi.org/10.1785/0120070026

Terzaghi, K. (1962). Measurement of stresses in rock. Institution of civil engineers. *Géotechnique*, *12*(2), 105-124.

Tveten, E., Lutro, O., & Thorsnes, T. (1998). *Berggrunnskart Ålesund. 1:250000, (Ålesund, western Norway)*. NGU Trondheim (bedrock map). Retrieved from https://www.ngu.no/publikasjon/alesund-berggrunnskart-alesund-m-1250-000-trykt-i-farger

Trnkoczy, A. (2012). Understanding and parameter setting of STA/LTA trigger algorithm. -In: *Bormann, P. (Ed.), New Manual of Seismological Observatory Practice, 2 (NMSOP-2),* Potsdam : Deutsches GeoForschungsZentrum, GFZ, 1-20. https://doi.org/0.2312/GFZ.NMSOP-2_IS_8.1

Viesca, R. C., & Rice, J. R. (2012). Nucleation of slip-weakening rupture instability in landslides by localized increase of pore pressure. *Journal of Geophysical Research: Solid Earth, 117*(B03104). https://doi.org/10.1029/2011JB008866

Voigtländer, A., Leith, K., & Krautblatter, M. (2018). Subcritical crack growth and progressive failure in Carrara marble under wet and dry conditions. *Journal of Geophysical Research: Solid Earth, 123*(5), 3780-3798. https://doi.org/10.1029/2017JB014956

Wei, M., Kaneko, Y., Liu, Y., & McGuire, J. J. (2013). Episodic fault creep events in California controlled by shallow frictional heterogeneity. *Nature Geoscience, 6*(7), 566-570. https://doi.org/10.1038/ngeo1835

Wesson, R. L. (1988). Dynamics of fault creep. *Journal of Geophysical Research: Solid Earth, 93*(B8), 8929-8951. https://doi.org/10.1029/JB093iB08p08929

Withers, M., Aster, R., Young, C., Beiriger, J., Harris, M., Moore, S., & Trujillo, J. (1998). A comparison of select trigger algorithms for automated global seismic phase and event detection. *Bulletin of the Seismological Society of America*, *88*(1), 95-106. https://doi.org/10.1785/BSSA0880010095

Yamada, M., Mori, J., & Matsushi, Y. (2016). Possible stick-slip behavior before the Rausu landslide inferred from repeating seismic events. *Geophysical Research Letters, 43*(17), 9038-9044. https://doi.org/10.1002/2016GL069288

Zhang, H., He, S., Liu, W., Deng, Y., & Hu, W. (2023). Creep-to-Runout Transition of Large Landslides Controlled by Frictional Velocity Strengthening and Weakening (Vajont 1963, Italy). *Rock Mechanics and Rock Engineering*, 56, 8471–8483. https://doi.org/10.1007/s00603-023-03473-2